

# Ellis-Bronnikov Wormhole Shadows with Spherically Symmetric Accretion Flow

Mikiya M. Takahashi<sup>1</sup> and Keisuke Nakashi<sup>2,3</sup>

<sup>1</sup>*Department of Liberal Arts, National Institute of Technology,  
Tokyo College, 1220-2, Kunugida-machi, Hachioji, Tokyo, 193-0942, Japan*

<sup>2</sup>*Kaichi Tokorozawa Secondary School, 169 Ohaza Matsugo,  
Tokorozawa City, Saitama 395-0015, Japan*

<sup>3</sup>*Department of Physics, Rikkyo University, Toshima, Tokyo 171-8501, Japan*

(Dated: June 2, 2026)

## Abstract

We investigate the observational differences between the Ellis–Bronnikov (EB) wormhole and the Schwarzschild black hole (BH) by performing general relativistic radiative transfer (GRRT) simulations. We consider a spherically symmetric steady-state accretion flow and perform GRRT simulations incorporating synchrotron emission. For both the EB wormhole and the Schwarzschild BH, the simulated images consist of a central shadow region and a bright photon ring. We find that both the shadow region and the photon ring of the EB wormhole are brighter than those of the Schwarzschild BH. These differences arise from the absence of an event horizon in the EB wormhole, allowing the emission from the accreting matter around and beyond the throat to contribute to the observed intensity. We also compare the simulated images with the Event Horizon Telescope (EHT) observations of M87\* and find that both the EB wormhole and the Schwarzschild BH are in reasonable agreement with the current EHT results.

## I. INTRODUCTION

Images of M87\* and Sgr A\* have been reported by the Event Horizon Telescope (EHT) Collaboration [1, 2]. The bright ring structures and associated shadows in the EHT images are produced by photons coming from the vicinity of the central compact object. Thus, the EHT images provide an important probe of the nature of strong gravitational fields around compact objects. The EHT data suggest that the central compact object is a Kerr black hole. However, the possibility that the central object is not a Kerr black hole has been actively discussed. The EHT Collaboration calculated images and broadband spectra in various spacetimes to constrain deviations from the Kerr metric [3], and concluded that compact objects with a thermal surface can be ruled out. On the other hand, the image size alone constrains deviations from the Kerr metric only at the  $\sim 10\%$  level [3]. This suggests that alternative models of the central compact object have not yet been fully ruled out by the current EHT observations. In fact, realistic images of a black hole with dilaton hair have been calculated using general relativistic magnetohydrodynamics (GRMHD) and general relativistic radiative transfer (GRRT) simulations [4, 5]. As a result, the authors pointed out that it is difficult to distinguish between the Kerr black hole and a dilatonic black hole from the images with the current EHT accuracy. Furthermore, it has also been pointed out that time variations in the radio flux and radio interferometry with extremely long baselines are useful for identifying the nature of compact objects [6, 7].

Beyond black holes with non-Kerr metrics, a variety of exotic compact objects have been proposed as alternative candidates that can produce shadow images remarkably similar to those of black holes. Among such candidates, wormholes have attracted attention as black hole mimickers. A wormhole is a horizonless compact object with a throat connecting two distant regions. In general relativity (GR), exotic matter that violates the null energy condition is required to sustain the wormhole structure [8, 9]. In this paper, we consider the Ellis–Bronnikov (EB) wormhole [10, 11], which is a traversable wormhole solution in GR supported by a massless phantom scalar field. The stability of the EB wormhole has been studied extensively. It is known that the EB wormhole is unstable against radial linear perturbations [12–16]. However, it has been shown that the instability can be mitigated by introducing additional matter fields [17–19] or by considering modified theories of gravity [20, 21].

Numerous previous studies have investigated the observational signatures of wormholes. In particular, their optical signatures have attracted considerable attention as a means of distinguishing wormholes from black holes. Gravitational lensing provides a powerful tool to probe the wormhole geometry. Gravitational lensing properties of the EB wormhole have been investigated, including gravitational microlensing and light curves [22–30], Einstein rings [31], and deflection angles in both the weak and strong deflection regimes [32–44]. More recently, motivated by the EHT observations, attention has shifted toward the direct imaging of wormholes, including their shadows and the images formed by surrounding accretion flows [45–58].

The observational appearance of the central compact object depends strongly on the properties of the accretion flow surrounding it, such as the geometry and optical depth of the accretion flow. In particular, Ohgami and Sakai [47] computed shadow images of the massless EB wormhole illuminated by a steady-state spherical dust flow. In the present paper, we extend their work to the EB wormhole and to more general spherically symmetric accretion flows. Unlike many previous studies in which the profiles of the accretion flow were prescribed by hand, we self-consistently derive the steady-state spherical flow solution in the EB wormhole spacetime. Furthermore, we calculate simulated images of the EB wormhole using GRRT simulations, taking into account realistic radiation processes such as synchrotron emission, and compare the resulting image structure with current EHT observations.

This paper is organized as follows. In Sec. II, we briefly review the EB wormhole solution and null and timelike geodesics. In Sec. III, we show the basic equations of the GRRT simulations and the numerical methodology to obtain the simulated image. In Sec. IV, we discuss the simulated images of the EB wormhole and the Schwarzschild black hole, and their differences. We also compare the resulting image structures with the current EHT results. We use the units  $c = G = h = 1$ .

## II. PROPERTIES OF ELLIS-BRONNIKOV WORMHOLE

### A. Theory and metric

We consider a massless phantom scalar field  $\Phi$  minimally coupled to GR. The action is given by

$$S = \frac{1}{16\pi} \int d^4x \sqrt{-g} [R + 8\pi(\nabla_\mu\Phi)(\nabla^\mu\Phi)]. \quad (1)$$

The field equations can be written as follows:

$$R_{\mu\nu} = -8\pi(\nabla_\mu\Phi)(\nabla_\nu\Phi), \quad (2)$$

$$\nabla_\mu\nabla^\mu\Phi = 0. \quad (3)$$

In this system, there is a class of static and spherically symmetric spacetimes known as the Ellis-Bronnikov (EB) wormhole. The phantom scalar field and the line element of the EB wormhole are given by

$$\Phi = \sqrt{\frac{M^2 + \ell^2}{4\pi\ell^2}} \left[ \tan^{-1} \left( \frac{R}{\ell} \right) - \frac{\pi}{2} \right], \quad (4)$$

$$ds^2 = -e^f dt^2 + e^{-f} [dR^2 + (R^2 + \ell^2)(d\theta^2 + \sin^2\theta d\phi^2)], \quad (5)$$

with

$$f(R) = \frac{2M}{\ell} \left[ \tan^{-1} \left( \frac{R}{\ell} \right) - \frac{\pi}{2} \right], \quad (6)$$

where  $\ell$  is a constant, and  $M$  is the ADM mass in the asymptotic flat region for  $R \rightarrow +\infty$ . We note that for  $R \rightarrow -\infty$ , the ADM mass of the EB wormhole is given by  $-e^{2\pi}M$ . This implies that the ADM mass associated with the  $R \rightarrow -\infty$  asymptotic flat region is negative if  $M$  is positive. In the EB wormhole, there are two asymptotic regions for  $R \rightarrow \pm\infty$ . These asymptotic regions are connected by a throat located at  $R_{\text{th}} = M$ . For  $R \rightarrow +\infty$ , since the function  $f$  goes to zero, the metric (5) reduces to the Minkowski metric. On the other hand, for  $R \rightarrow -\infty$ , the metric coincides with the Minkowski metric after the following coordinate

transformations:

$$\tilde{t} := e^{-\pi M/\ell} t, \quad \tilde{R} := e^{\pi M/\ell} R, \quad \tilde{\ell} := e^{\pi M/\ell} \ell. \quad (7)$$

For  $M = 0$ , the EB wormhole describes a symmetric wormhole, which is called the Ellis wormhole. The metric of the Ellis wormhole is given by

$$ds^2 = -dt^2 + dR^2 + (R^2 + \ell^2)(d\theta^2 + \sin^2 \theta d\phi^2). \quad (8)$$

In the Ellis wormhole, a throat is located at  $R = 0$ . Images of the Ellis wormhole illuminated by steady-state spherical dust fluids have been reported in [47]. In this paper, we extend this analysis to the EB wormhole ( $M \neq 0$ ), considering illumination by steady-state spherical polytropic fluids.

## B. Geodesics and circular orbits

Here, we analyze geodesics of freely falling test particles in the EB wormhole. In this subsection, we consider particles moving in the equatorial plane, i.e.,  $\theta = \pi/2$ .

The Lagrangian of a test particle is defined by

$$2\mathcal{L} = g_{\mu\nu} \dot{x}^\mu \dot{x}^\nu = -\epsilon, \quad (9)$$

where the dot denotes derivatives with respect to an affine parameter, and  $\epsilon = 1$  for a timelike particle, while  $\epsilon = 0$  for a massless particle. Due to the symmetries of the spacetime, there are two Killing vectors  $(\partial_t)^\mu$  and  $(\partial_\phi)^\mu$ . As a result, the energy  $E$  and the angular momentum  $L$  of a particle are conserved, and the constants of motion are given by

$$E = e^f \dot{t}, \quad L = e^{-f} (R^2 + \ell^2) \dot{\phi}. \quad (10)$$

From the normalization of the four velocity, we introduce the effective potential as follows:

$$\dot{R}^2 + V_{\text{eff}}(R) = E^2, \quad (11)$$

$$V_{\text{eff}}(R) := e^f \left( \epsilon + e^f \frac{L^2}{R^2 + \ell^2} \right). \quad (12)$$

We analyze circular orbits for a particle. A particle in a circular orbit satisfies  $\dot{R} = 0$  and  $\ddot{R} = 0$ . The condition  $\dot{R} = 0$  leads to

$$V_{\text{eff}} = E^2. \quad (13)$$

On the other hand, the condition  $\ddot{R} = 0$  leads to

$$V'_{\text{eff}} = 0, \quad (14)$$

where the prime denotes the derivative with respect to  $R$ . Therefore, the locations of the circular orbits correspond to those of the stationary points of  $V_{\text{eff}}$ .

For timelike particles ( $\epsilon = 1$ ), combining Eqs. (13) and (14), we can find the energy and the angular momentum of a circular orbit as

$$E_c^2 := e^f \frac{R - M}{R - 2M}, \quad (15)$$

$$L_c^2 := e^{-f} \frac{M(R^2 + \ell^2)}{R - 2M}. \quad (16)$$

Due to the strong gravitational nature of the EB wormhole, there are unstable circular orbits as well as stable circular orbits. The positions of the stable and the unstable circular orbits correspond to the local minimum and maximum of  $V_{\text{eff}}$ , respectively. There is a radius at which a sequence of stable circular orbits switches to a sequence of unstable circular orbits. Such a radius is called the innermost stable circular orbit (ISCO). The position of the ISCO corresponds to the inflection point of  $V_{\text{eff}}$ , and the following condition is satisfied:

$$V''_{\text{eff}}|_{\text{ISCO}} = 0. \quad (17)$$

In the EB wormhole, the ISCO radius is given by

$$R_{\text{ISCO}} = 3M + \sqrt{\ell^2 + 5M^2}. \quad (18)$$

Next, we discuss massless particles. The conditions for a circular orbit of a massless particle are the same as in the timelike particle case, i.e.,  $\dot{R} = \ddot{R} = 0$ . The effective potential of a massless particle is

$$V_{\text{eff}} = e^{2f} \frac{b^2}{R^2 + \ell^2}, \quad (19)$$

where  $b := L/E$  is the impact parameter. We note that a circular orbit of a massless particle is called the photon sphere. Since the radius of the photon sphere corresponds to the local maximum of  $V_{\text{eff}}$ , we obtain the radius of the photon sphere from  $V'_{\text{eff}} = 0$  as follows:

$$R_{\text{ps}} := 2M. \quad (20)$$

In addition, by imposing the conditions  $\dot{R} = \ddot{R} = 0$ , the critical impact parameter for a massless particle that asymptotically approaches the photon sphere is given by

$$b_{\text{ps}} := e^{-\frac{2M}{\ell} [\tan^{-1}(2M/\ell) - \pi/2]} \sqrt{4M^2 + \ell^2}. \quad (21)$$

### III. METHOD

#### A. General relativistic radiative transfer equation

The GRRT equation is described as

$$\frac{d\mathcal{I}}{d\lambda} = \mathcal{J} - \mathcal{A}\mathcal{I}, \quad (22)$$

where  $\lambda, \mathcal{I}, \mathcal{J}$  and  $\mathcal{A}$  are an affine parameter, the invariant intensity, invariant emissivity, and invariant absorption coefficient, respectively [59, 60]. Here,  $d\lambda$  is related to the line element  $ds$  as  $ds = \nu d\lambda$ , where  $\nu$  is a frequency measured in a local Minkowski frame. The

invariant variables are defined by

$$\mathcal{I} := \frac{I_\nu}{\nu^3}, \quad (23)$$

$$\mathcal{J} := \frac{j_\nu}{\nu^2}, \quad (24)$$

$$\mathcal{A} := \nu \kappa_\nu, \quad (25)$$

where  $I_\nu$ ,  $j_\nu$ , and  $\kappa_\nu$  are the intensity, the emissivity, and the absorption coefficient measured in a local Minkowski frame, respectively. By substituting  $\mathcal{I} = I_{\nu_{\text{obs}}}/\nu_{\text{obs}}^3$ ,  $ds = \nu_{\text{obs}}d\lambda$  on the left-hand side and  $\mathcal{I} = I_{\nu_{\text{rest}}}/\nu_{\text{rest}}^3$ ,  $\mathcal{J} = j_{\nu_{\text{rest}}}/\nu_{\text{rest}}^2$ ,  $\mathcal{A} = \nu_{\text{rest}}\kappa_{\nu_{\text{rest}}}$  on the right-hand side of Eq. (22), the GRRT equation can be written as

$$\frac{dI_{\nu_{\text{obs}}}}{ds} = g^3 (j_{\nu_{\text{rest}}} - \kappa_{\nu_{\text{rest}}} I_{\nu_{\text{rest}}}), \quad (26)$$

where  $I_{\nu_{\text{obs}}}$  is the observed intensity on the screen, while  $I_{\nu_{\text{rest}}}$ ,  $j_{\nu_{\text{rest}}}$ , and  $\kappa_{\nu_{\text{rest}}}$  are the intensity, the emissivity, and the absorption coefficient in the fluid rest frame, respectively. Here,  $g := \nu_{\text{obs}}/\nu_{\text{rest}}$  is the redshift factor, which represents the frequency shift including both the gravitational redshift and the Doppler shift by the fluid motion, where  $\nu_{\text{obs}}$  and  $\nu_{\text{rest}}$  are the photon frequencies in the observer's frame and the fluid rest frame, respectively. Furthermore, we ignore the synchrotron self-absorption (i.e.,  $\kappa_{\nu_{\text{rest}}} = 0$ ) because we assume that the accretion flows are sufficiently optically thin.

In this work, we assume that the accreting matter emits synchrotron radiation. The angle-averaged thermal synchrotron emissivity in the fluid rest frame is approximated by [61]<sup>1</sup>

$$j_{\nu_{\text{rest}}} = \frac{n_e e^2 \nu_{\text{rest}}}{\sqrt{3} K_2(\Theta_e^{-1})} \mathcal{M}(w_{\text{cs}}), \quad (27)$$

where  $n_e$  is the electron number density,  $e$  is the electric charge, and  $K_2$  is the modified Bessel function of the second kind. The dimensionless electron temperature is defined as  $\Theta_e := k_B T_e / m_e$ , with  $T_e$  and  $m_e$  being the electron temperature and mass, respectively. The

---

<sup>1</sup> This formula is widely used for simulating radio images of compact objects (e.g., [62–67]).

function  $\mathcal{M}(w_{\text{cs}})$  is given by

$$\mathcal{M}(w_{\text{cs}}) = \frac{4.0505}{w_{\text{cs}}^{1/6}} \left( 1 + \frac{0.4}{w_{\text{cs}}^{1/4}} + \frac{0.5316}{w_{\text{cs}}^{1/2}} \right) \exp(-1.8899w_{\text{cs}}^{1/3}), \quad (28)$$

where  $w_{\text{cs}} := \nu_{\text{rest}}/\nu_{\text{cs}}$  is the frequency normalized by the characteristic synchrotron frequency  $\nu_{\text{cs}} := 3eB_{\text{mag}}\Theta_e^2/4\pi m_e$ , and  $B_{\text{mag}}$  is the magnetic field strength measured in the fluid rest frame. The magnetic field strength is derived from the energy equipartition as

$$B_{\text{mag}} = \sqrt{\frac{8\pi n_e k_B T_e}{\beta_p}}, \quad (29)$$

where  $\beta_p$  is the plasma beta, which is the ratio of the gas pressure to the magnetic pressure. We set  $\beta_p = 0.1$  throughout this paper.

## B. Numerical setup

We simulate the shadow images of the Schwarzschild BH and the EB wormhole. For the Schwarzschild BH, we adopt a mass of  $M = 6.2 \times 10^9 M_\odot$ , where  $M_\odot$  denotes the solar mass, which we refer to as the fiducial mass. We also calculate the shadow image of the EB wormhole with the fiducial mass, and find that its shadow size is larger than that of the Schwarzschild BH. To match the shadow size of the EB wormhole with that of the Schwarzschild BH, we also consider the EB wormhole with  $M = 5.27 \times 10^9 M_\odot$ , which we refer to as the low-mass EB wormhole. In addition, we set  $\ell = 2M$  in Eq. (5). For all cases, the distance to the object is set to  $D = 16.7$  Mpc, motivated by the distance to M87\* [68–70].

We obtain a solution of a spherically symmetric steady-state transonic accretion flow onto the Schwarzschild BH and the EB wormhole as discussed in Appendix A. We assume polytropic fluids with  $\Gamma = 4/3$ , where  $\Gamma$  is the adiabatic index. We also assume that the accretion flow lies in the range  $-15M < R < 15M$  for the EB wormhole, while in the range  $2M < R < 15M$  for the Schwarzschild BH. There is no the accretion flow outside these ranges. For both the Schwarzschild BH and the EB wormhole, the electron number density, the temperature, the magnetic field strength, and the Lorentz factor are shown in Fig. 1. The maximum values of the electron number density and the electron temperature are set

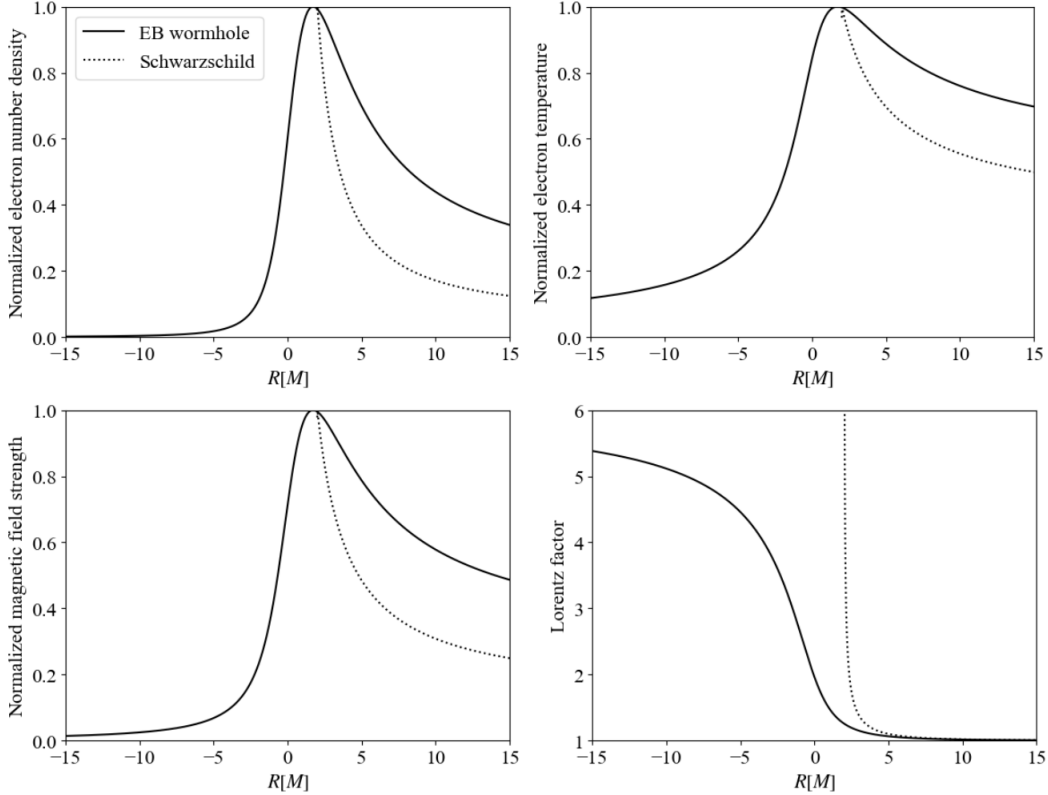


FIG. 1. Distributions of the electron number density (top left), the electron temperature (top right), the magnetic field strength (bottom left), and the Lorentz factor (bottom right). The solid and dotted curves correspond to the EB wormhole and the Schwarzschild BH cases, respectively. The electron number density, the electron temperature, and the magnetic field strength are normalized by their respective maximum values.

to  $1.7 \times 10^5 \text{ cm}^{-3}$  and  $5.0 \times 10^{10} \text{ K}$  for the fiducial-mass EB wormhole,  $2.4 \times 10^5 \text{ cm}^{-3}$  and  $5.0 \times 10^{10} \text{ K}$  for the low-mass EB wormhole, and  $5.6 \times 10^5 \text{ cm}^{-3}$  and  $1.0 \times 10^{11} \text{ K}$  for the Schwarzschild BH, respectively. These parameters are chosen so that the total flux of the image is approximately  $0.5 \text{ Jy}^2$ , and are approximately consistent with those estimated from the EHT polarization observations [71, 72].

To integrate the geodesic equation and generate realistic EB wormhole images, we use the GRRT code: `CARTOON` [60]. The geodesic equation is integrated backward in time along the geodesic from the observer’s screen which is located at  $R = 1000M$ . The interval along the geodesic (i.e., time step to integrate the geodesic equation),  $\Delta s = \nu \Delta \lambda$ , is set to be  $10^{-2}M$ . The viewing angle of the observer is arbitrary because both the spacetime and the accretion flow are spherically symmetric. The screen spans  $-10M \leq X, Y \leq 10M$ , where

<sup>2</sup> “Jy” is a unit of flux density ( $1 \text{ Jy} = 10^{-23} \text{ erg} \cdot \text{s}^{-1} \cdot \text{cm}^{-2} \cdot \text{Hz}^{-1}$ ).

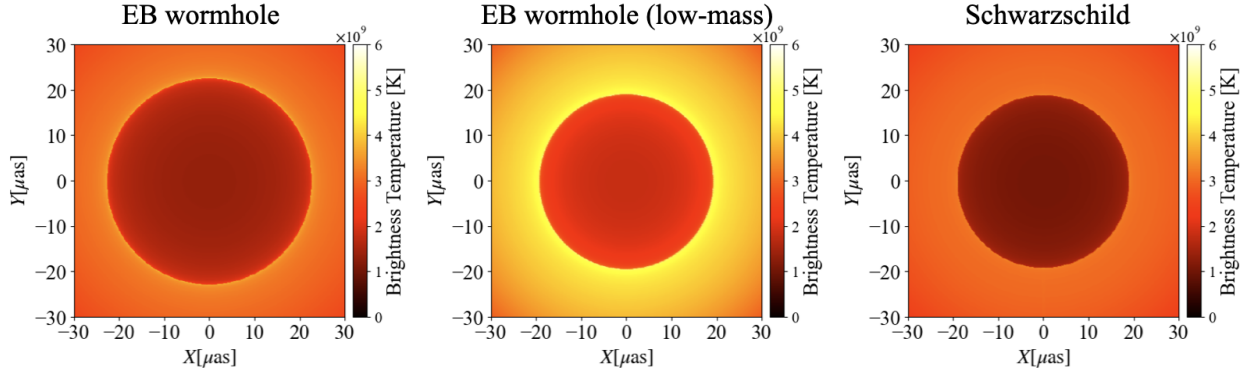


FIG. 2. Simulated images of the EB wormhole (left), the low-mass EB wormhole (center), and the Schwarzschild BH (right), respectively. The color denotes the brightness temperature  $T_b := I_{\nu_{\text{obs}}} / (2\nu_{\text{obs}}^2 k_B)$ .

$X$  and  $Y$  are the horizontal and the vertical axes, and is uniformly divided into  $512 \times 512$  pixels. We integrate the geodesic equations backward in time from the center of each pixel on the screen. We also assume that the observed frequency is  $\nu_{\text{obs}} = 230$  GHz.

## IV. RESULTS

### A. Simulated images

Figure. 2 shows the simulated images for the fiducial-mass EB wormhole (left panel), the low-mass EB wormhole (center panel), and the Schwarzschild BH (right panel). The color scale represents the brightness temperature defined by  $T_b := I_{\nu_{\text{obs}}} / (2\nu_{\text{obs}}^2 k_B)$ . All images exhibit a central dark region, referred to as the shadow region, and a bright ring-like structure, referred to as the photon ring. The shadow region is formed by the photons with angular momenta smaller than those of photons on the unstable circular orbit. On the other hand, the photon ring is formed by the photons orbiting around the central object multiple times before reaching the observer. The diameter of the photon ring for the fiducial-mass EB wormhole is greater than that of the Schwarzschild BH. For the Schwarzschild BH, the radius of the photon ring is  $3\sqrt{3}M \sim 5.19M$ , while for the EB wormhole, the radius is about  $6.21M$ .

Figure 3 shows the intensity profiles along the  $Y = 0$  for the EB wormhole cases (solid and dashed curves) and the Schwarzschild BH case (dotted curve). There are notable differences between the EB wormhole cases and the Schwarzschild BH case. The EB wormhole images

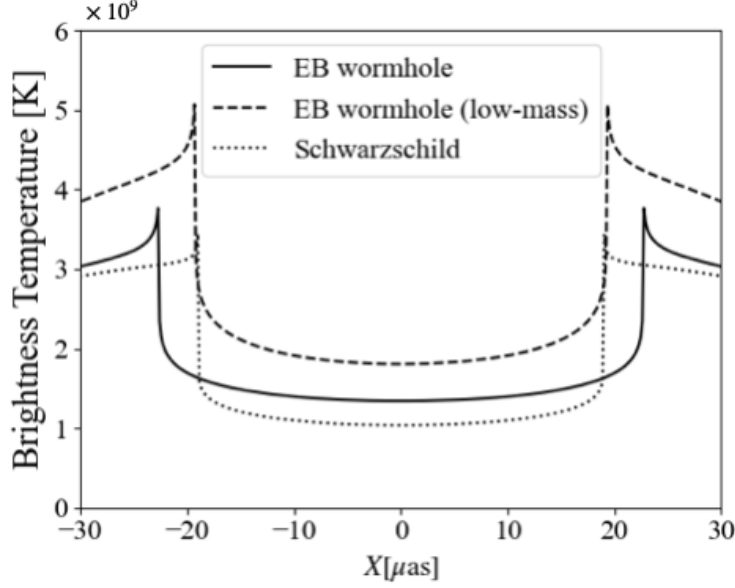


FIG. 3. Intensity profiles along the  $Y = 0$  of the simulated images shown in Fig. 2. The solid, dashed, and dotted curves are the EB wormhole case, the low-mass EB wormhole case, and the Schwarzschild BH case, respectively.

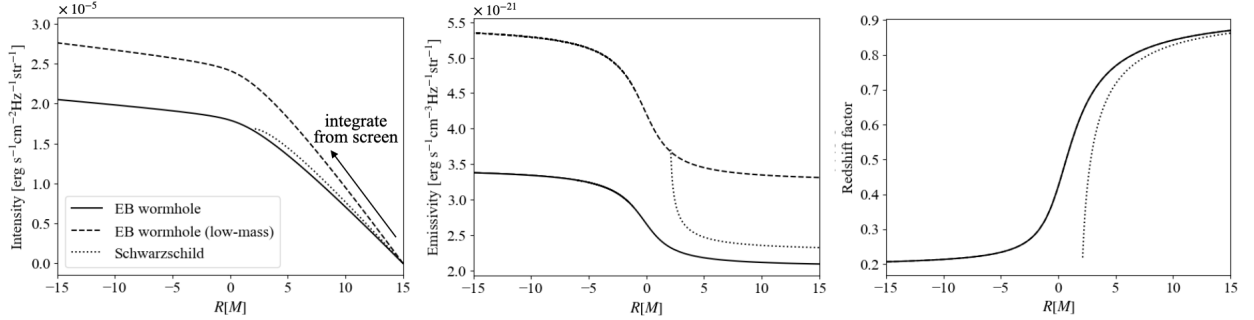


FIG. 4. The observed intensity (left), the emissivity in the fluid rest frame (center), and the redshift factor (right) along the geodesic of a photon that reaches the center of the screen. The solid, dashed, and dotted curves represent the cases of the EB wormhole, the low-mass EB wormhole, and the Schwarzschild BH, respectively.

are brighter than the Schwarzschild BH image, both in the shadow region and at the photon ring.

The higher brightness of the shadow region in the EB wormhole can be understood as follows. Figure 4 shows the intensity  $I_{\nu_{\text{obs}}}$ , the emissivity in the fluid rest frame  $j_{\nu_{\text{rest}}}$ , and the redshift factor  $g$  along a null geodesic reaching the center of the screen  $(X, Y) = (0, 0)$ . Since we integrate the GRRT equation backward in time from the screen, the intensity is zero at the screen and increases as the integration proceeds backward in time, so that the left end

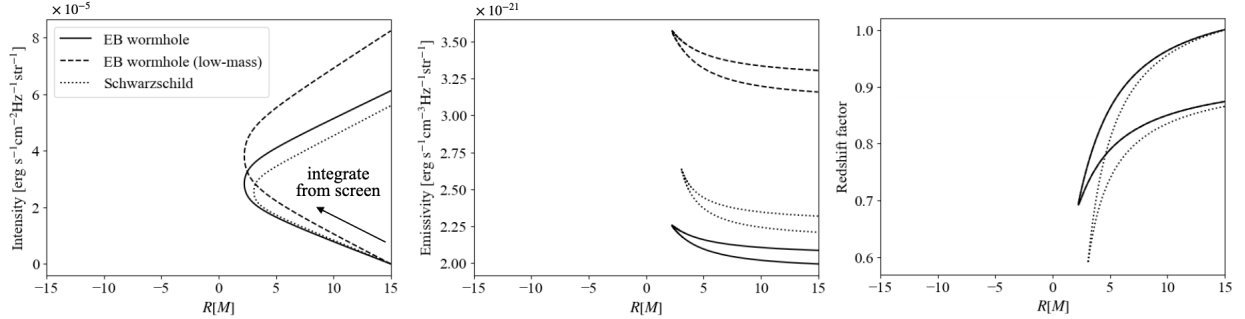


FIG. 5. The observed intensity (left), the emissivity in the fluid rest frame (center), and the redshift factor (right) along the geodesic of a photon that produces the peak intensity. The solid, dashed, and dotted curves represent the cases of the EB wormhole, the low-mass EB wormhole, and the Schwarzschild BH, respectively.

of each curve corresponds to the observed intensity. For the fiducial-mass case, in the region outside the event horizon of the Schwarzschild BH, the intensity for the Schwarzschild BH is greater than that for the EB wormhole (see the left panel of Fig. 4). This is because the synchrotron emissivity for the Schwarzschild BH is larger than that for the EB wormhole in this region (see the center panel of Fig. 4), and this effect dominates over the smaller redshift factor of the Schwarzschild BH case compared with the EB wormhole case (see the right panel of Fig. 4). However, the observed intensity in the shadow region for the EB wormhole is higher than that for the Schwarzschild BH. This is because, in the EB wormhole case, the accreting matter exists not only in the vicinity of the throat but also beyond it, owing to the absence of the event horizon. The emission from this accreting matter beyond the throat contributes to the observed intensity, resulting in the higher brightness in the shadow region compared with the Schwarzschild BH case.

Next, we discuss why the photon ring of the EB wormhole is brighter than that of the Schwarzschild BH. To this end, we focus on the null geodesic with the largest bending angle, which produces the peak intensity. Figure 5 shows the observed intensity  $I_{\nu_{\text{obs}}}$ , the emissivity in the fluid rest frame  $j_{\nu_{\text{rest}}}$ , and the redshift factor  $g$  along such a null geodesic. The turning points seen in Fig. 5 reflect the trajectories of the geodesics: traveling from the light source, approaching and orbiting the central object several times near the photon sphere, and finally propagating outward to reach the screen. In the fiducial-mass case, although the emissivity along the geodesic for the Schwarzschild BH is larger than that for the EB wormhole (see the center panel of Fig. 5), the photon ring of the EB wormhole is brighter than that of the Schwarzschild BH, as seen in the left panel of Fig. 5. There are two main reasons for this.

	Total flux [Jy]	Ring diameter [ $\mu\text{as}$ ]	Central depression
EHT M87*	0.2–1.2 [72]	$42 \pm 3$ [1]	$\sim 10$ [1]
EBWH	0.51	$\simeq 45$	$\simeq 2.8$
Low-mass EBWH	0.50	$\simeq 38$	$\simeq 2.8$
Schwarzschild BH	0.50	$\simeq 38$	$\simeq 1.9$

TABLE I. The total flux, the ring diameter, and the central depression of the EHT M87\* result and our simulated images.

The first is that the path length of the photon for the EB wormhole is longer than that for the Schwarzschild BH. Specifically, the path length of the photon in the EB wormhole case is longer than that in the Schwarzschild BH case; the difference in the coordinate time along the geodesic is  $\Delta t \sim 3.4M^3$ . The second is the smaller redshift factor in the Schwarzschild BH case compared with the EB wormhole case as shown in the right panel of Fig. 5. Even a small difference in the redshift factor can result in a significant difference in the observed intensity, since the intensity scales as  $g^3$  in the GRRT equation (26).

The above discussion remains the same for the low-mass EB wormhole, which has the same size shadow as the Schwarzschild BH. For the low-mass EB wormhole, the observed intensity in both the shadow region and the photon ring becomes larger than that of the Schwarzschild BH, because the emissivity is several times greater than that in the Schwarzschild BH case.

We note that the simulated image of the Ellis wormhole is discussed in Appendix B. For the Ellis wormhole, the region inside the photon ring is brighter than the region outside the photon ring. This trend is consistent with the previous work [47].

## B. Comparison with EHT observations

Here, we compare several observables derived from our simulated images with the EHT results. Table I shows the total flux, the ring diameter, and the central depression (the ratio of the maximum to the minimum intensity) of our simulated images and the EHT result for M87\*. At least within the numerical model adopted in this paper, we find no significant difference in the image features between the EB wormhole and the Schwarzschild BH. Furthermore, the observables of our simulated images are broadly consistent with the

<sup>3</sup> The affine parameter length in the EB wormhole case is also longer than that in the Schwarzschild BH case by approximately  $9.1M$ .

EHT results for M87\*.

We note that the central depression of our simulated images tends to be smaller than that inferred from the EHT result when we assume that the fluid distribution is spherically symmetric. For the axisymmetric fluid distribution, which corresponds to a more realistic situation, it is expected that the intensity of photons whose angular momentum is aligned with that of the accretion flow becomes greater via the Doppler boosting. In contrast, the intensity of photons whose angular momentum is in the opposite direction to that of the matter is suppressed by the Doppler deboosting. As a result, when there is an axisymmetric fluid distribution, the image structure becomes asymmetric, and the ratio of the maximum to the minimum intensity is enhanced.

## V. SUMMARY AND DISCUSSION

In this paper, we have calculated the shadow images of the EB wormhole and the Schwarzschild BH for spherically symmetric steady-state transonic accretion flows. We have taken into account the synchrotron emission and solved the GRRT equation to obtain realistic shadow images. For both the EB wormhole and the Schwarzschild BH, the images consist of the central dark region (shadow region) and a bright ring-like structure (photon ring). We have found that when the mass is fixed, the shadow region for the EB wormhole is brighter than that for the Schwarzschild BH. This is because the photons emitted by the accreting matter that exists not only in the vicinity of the throat but also beyond it can contribute to the observed intensity in the EB wormhole case. In addition, we have found that the photon ring is also brighter for the EB wormhole than for the Schwarzschild BH. This is because the path length of the photon that generates the photon ring in the EB wormhole spacetime is longer than that in the Schwarzschild BH spacetime, and the redshift factor in the vicinity of the EB wormhole is larger than that near the Schwarzschild BH. In the EB wormhole, the lapse function does not vanish near the object because there is no event horizon, unlike the Schwarzschild BH. Thus, the resulting intensity of the photon ring in the EB wormhole case tends to be larger than that in the Schwarzschild BH case.

We have compared the features of the simulated images with the current EHT results for M87\*. We have found that the image features, which are the total flux, the ring diameter, and the ratio of the maximum to minimum intensity, are broadly consistent with the EHT

results, and conclude that there is no significant discrepancy between the EB wormhole image features and the EHT results, at least within the numerical setup adopted in this paper. In order to distinguish the EB wormhole from a BH spacetime, observations with sufficiently high angular resolution are required. A promising candidate for such high-resolution observations is a space-VLBI observation, such as the “Black Hole Explorer” (BHEX) mission [73–75] planned for the early 2030s.

Simulations of more realistic images, taking into account more realistic fluid distributions, are left for future work. Furthermore, in reality, an axisymmetric accretion flow (accretion disk) forms around the compact object. When an accretion disk exists around the compact object, an asymmetric intensity distribution is expected to be realized. Furthermore, in the future, it is also possible to carry out calculations that take into account a more realistic structure of the accretion flow using GRMHD simulations.

## ACKNOWLEDGMENTS

Our numerical simulations were conducted with HPE Cray XD2000 at the Center for Computational Astrophysics, National Astronomical Observatory of Japan. This work was supported by Takahashi Industrial and Economic Research Foundation and JSPS KAKENHI Grant Numbers 25K01045, 26K17201 (MMT).

## Appendix A: Details of accretion flows

### 1. Thermodynamics

We assume the flow to be adiabatic and free of dissipative processes. The entropy per particle  $\sigma$  is therefore conserved along the flow:  $u^\mu \nabla_\mu \sigma = 0$ , where  $u^\mu$  is the four-velocity of the fluid. For an adiabatic fluid, the first law of thermodynamics can be written as

$$d\left(\frac{\rho}{n}\right) = -p d\left(\frac{1}{n}\right), \quad (\text{A1})$$

where  $\rho$ ,  $p$ ,  $n$  are the total energy density, the pressure, and the number density measured in the fluid rest frame, respectively. Eq. (A1) leads to the following relations

$$dp = ndh, \quad d\rho = hdn, \quad (\text{A2})$$

where  $h$  is the enthalpy per particle defined by

$$h := \frac{\rho + p}{n}. \quad (\text{A3})$$

For the later discussion, we introduce the sound speed of the fluid. Since we consider the adiabatic flow, the sound speed can be expressed as

$$a^2 := \frac{dp}{d\rho} = \frac{d \ln h}{d \ln n}, \quad (\text{A4})$$

where we used Eq. (A2).

## 2. Steady-state accretion flows in a static and spherically symmetric spacetime

We consider a static and spherically symmetric spacetime described by the following metric:

$$ds^2 = -A(R)dt^2 + B(R)dR^2 + C(R)(d\theta^2 + \sin^2\theta d\phi^2). \quad (\text{A5})$$

In addition, we consider a perfect fluid whose energy-momentum tensor is given by

$$T^{\mu\nu} = (\rho + p)u^\mu u^\nu + pg^{\mu\nu}. \quad (\text{A6})$$

Since we focus on a spherically symmetric steady-state accretion flow, the four-velocity of the fluid satisfies  $u^\mu = (u^t, u^R, 0, 0)$ .

Here, we introduce an orthonormal tetrad  $\{e^\mu_{\hat{\alpha}}\}$  attached to a static observer. The tetrad is given by

$$e^\mu_{\hat{\alpha}} = \text{diag} \left( \frac{1}{\sqrt{A}}, \frac{1}{\sqrt{B}}, \frac{1}{\sqrt{C}}, \frac{1}{\sqrt{C} \sin \theta} \right). \quad (\text{A7})$$

This tetrad satisfies  $\eta_{\hat{\alpha}\hat{\beta}} = g_{\mu\nu}e^{\mu}_{\hat{\alpha}}e^{\nu}_{\hat{\beta}}$ , where  $\eta_{\hat{\alpha}\hat{\beta}}$  is the Minkowski metric. The four-velocity measured by a static observer is obtained by projection onto the tetrad as  $u^{\hat{\alpha}} = e^{\hat{\alpha}}_{\mu}u^{\mu}$ . In the local frame of a static observer, the four-velocity takes the special relativistic form

$$u^{\hat{\alpha}} = (\gamma, \gamma v, 0, 0), \quad (\text{A8})$$

where  $\gamma := (1 - v^2)^{-1/2}$  is the Lorentz factor and

$$v := \frac{u^{\hat{r}}}{u^{\hat{t}}} = \sqrt{\frac{B}{A}} \frac{u^R}{u^t} \quad (\text{A9})$$

is the radial velocity of the fluid measured by a static observer.

Assuming that the number density of particles is conserved, we can find a conserved quantity from the continuity equation  $\nabla_{\mu}(nu^{\mu}) = 0$  as

$$\dot{N} := -4\pi\sqrt{A}Cn\gamma v, \quad (\text{A10})$$

where we define the sign of  $\dot{N}$  such that  $\dot{N}$  is positive for the accretion flow in which  $v < 0$ . Since we consider the static and spherically symmetric spacetime, there is another conserved quantity associated with the timelike Killing vector  $(\partial_t)^{\mu}$ . With the timelike Killing vector  $(\partial_t)^{\mu}$ , the Noether current is given by  $J^{\mu} := -T^{\mu}_{\nu}(\partial_t)^{\nu}$ . From the conservation equation for the Noether current  $\nabla^{\mu}J_{\mu} = 0$ , we can find the conserved quantity as

$$\mathcal{E}^2 := h^2\gamma^2 A. \quad (\text{A11})$$

This quantity represents the relativistic generalization of the Bernoulli constant and reduces to the classical Bernoulli constant in the Newtonian limit.

The solutions of the flow are described as the curves in the phase space  $(R, v)$ . These solutions can be obtained by integrating the following equations:

$$\frac{d}{d\tau} \begin{pmatrix} R \\ v \end{pmatrix} = \begin{pmatrix} \partial_v \\ -\partial_R \end{pmatrix} \mathcal{E}^2(R, v), \quad (\text{A12})$$

where  $\tau$  is a parameter characterizing the curves. At the critical point, the right-hand side

of Eq. (A12) vanishes. This leads to

$$\frac{2Ah^2}{v(1-v^2)^2}(v^2 - a^2) = 0, \quad (\text{A13})$$

$$\frac{2Ah^2}{1-v^2} \left( \frac{1-a^2}{2} \frac{A'}{A} - a^2 \frac{C'}{C} \right) = 0. \quad (\text{A14})$$

From Eq. (A13), it follows that  $v^2 = a^2$  at the critical point. In other words, the critical point coincides with the sonic point. In what follows, we use the notation  $(R_c, v_c)$  to denote the critical point. We can classify the critical point into two types, i.e., a saddle type or an extremum type. In this study, we consider an accretion flow that vanishes at the  $R \rightarrow +\infty$ , transitions from subsonic to supersonic at the sonic point, and then flows into the  $R < 0$  region. Such accretion flows can be realized when the critical points are saddle type.

### 3. Application to polytropic fluid

In the present paper, we consider polytropic fluids as an explicit example. The equation of state (EOS) for polytropic fluids is given by

$$p = Kn^\Gamma, \quad (\text{A15})$$

where  $K$  is a constant that is determined by the thermodynamic properties of the fluid, while  $\Gamma$  is the adiabatic index. In order to calculate a shadow image, we need to find the temperature, the number density, and the radial velocity. For the adiabatic fluids, the energy density can be written as

$$\rho = mn + \frac{p}{\Gamma - 1}, \quad (\text{A16})$$

where  $m$  is a mass of an accreting particle. Substituting Eq. (A16) into Eq. (A3), we find the pressure as follows:

$$p = \frac{\Gamma - 1}{\Gamma} n (h - m). \quad (\text{A17})$$

By using the EOS  $p = nk_B T$ , we finally obtain the expression for the temperature

$$T = \frac{\Gamma - 1}{k_B \Gamma} \left( \frac{\mathcal{E}}{\gamma \sqrt{A}} - m \right), \quad (\text{A18})$$

where we used Eq. (A11). The number density can be calculated from Eq. (A10):

$$n = -\frac{\dot{N}}{4\pi\sqrt{AC}\gamma v}. \quad (\text{A19})$$

Therefore, we can calculate the temperature and the number density if we find the radial velocity  $v$ . To find the radial velocity, we need to solve the following differential equation

$$\frac{dv}{dR} = \frac{-\partial_R \mathcal{E}^2}{\partial_v \mathcal{E}^2}. \quad (\text{A20})$$

To construct the global transonic solution, we first determine the radial velocity at the sonic point. The slope at the sonic point is obtained from a linear analysis of the flow equations. Using these values, we slightly shift the radial position to both sides of the sonic point and integrate the equations inward and outward to obtain the full radial velocity profile.

To classify the accretion flows, we linearize the dynamical system around the critical point by expanding the solution as  $(R, v) = (R_c + \delta R, v_c + \delta v)$ . Expanding Eq. (A12) around the critical point, the linearized equation is given by

$$\frac{d}{d\tau} \begin{pmatrix} \delta R \\ \delta v \end{pmatrix} = \mathcal{J} \begin{pmatrix} \delta R \\ \delta v \end{pmatrix}, \quad (\text{A21})$$

where we introduced the linearization matrix  $\mathcal{J}$  defined by

$$\mathcal{J} := \begin{pmatrix} \partial_R \partial_v & \partial_v^2 \\ -\partial_R^2 & -\partial_R \partial_v \end{pmatrix} \mathcal{E}^2(R_c, v_c). \quad (\text{A22})$$

The nature of the critical point is determined by the eigenvalues of the linearization matrix. If the eigenvalues are real and have opposite signs, the critical point is of saddle type. Therefore,  $\det \mathcal{J} < 0$  is required for realizing transonic accretion flows. In this case, there exist two distinct directions in phase space along which the flow can pass through the critical point. By contrast, if the eigenvalues have the same sign or form a complex conjugate pair,

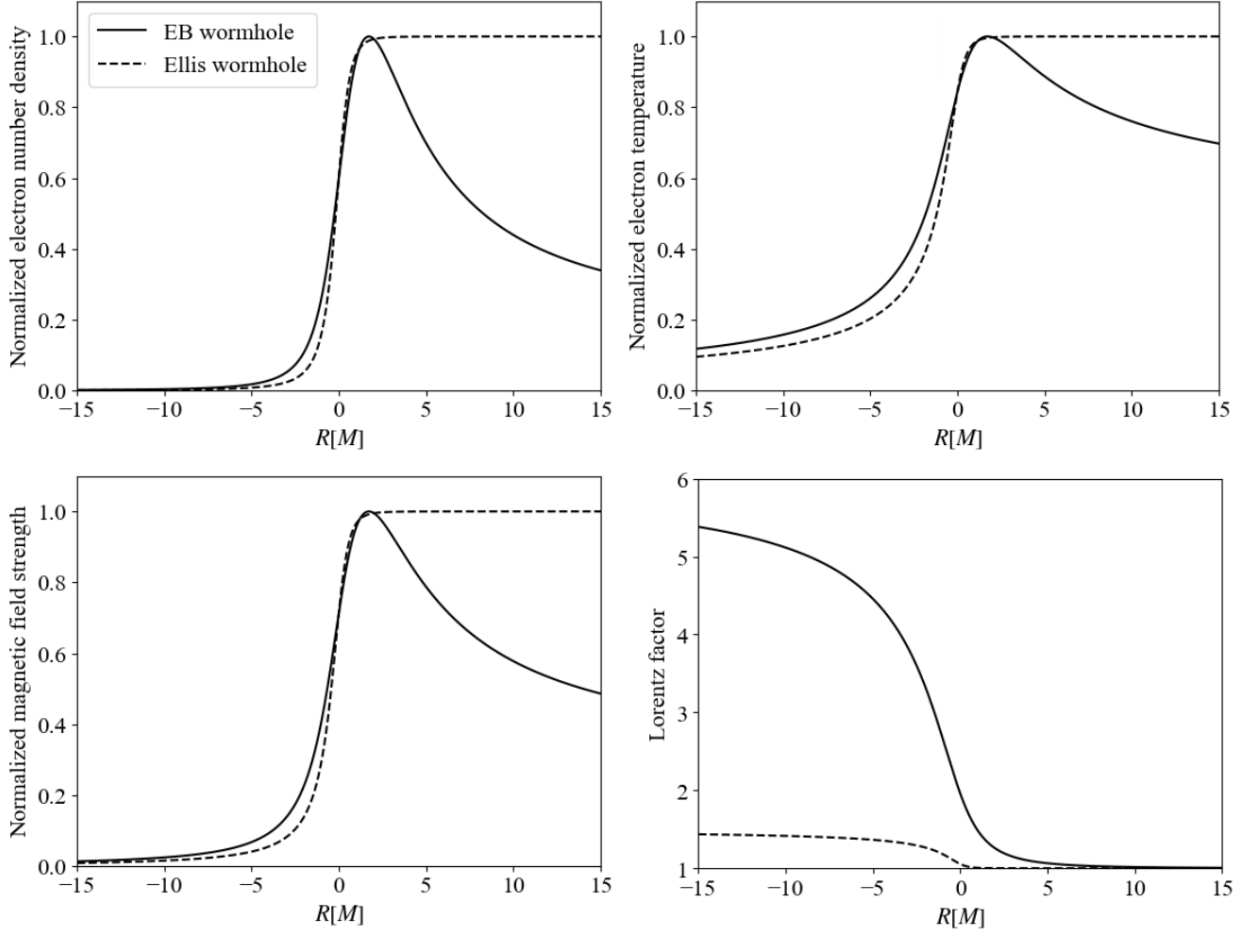


FIG. 6. Distributions of the electron number density (top left), the electron temperature (top right), the magnetic field strength (bottom left), and the Lorentz factor (bottom right). The solid and dashed curves correspond to the EB wormhole case and the Ellis wormhole case, respectively. The electron number density, the electron temperature, and the magnetic field strength are normalized by their respective maximum values.

the flow cannot represent a physically viable transonic accretion flows passing through the critical point.

## Appendix B: Image of the Ellis wormhole

To assess the effect of differences in fluid distributions between our study and the previous study [47], we calculated the image of the Ellis wormhole. In [47], the dust fluid in the Ellis wormhole spacetime was considered. The steady-state spherical dust solution can be described by a constant velocity solution. The authors have denoted the constant velocity as  $u_\infty$ . If  $u_\infty$  vanishes, the number density  $n$  becomes an arbitrary function of  $R$ . However,

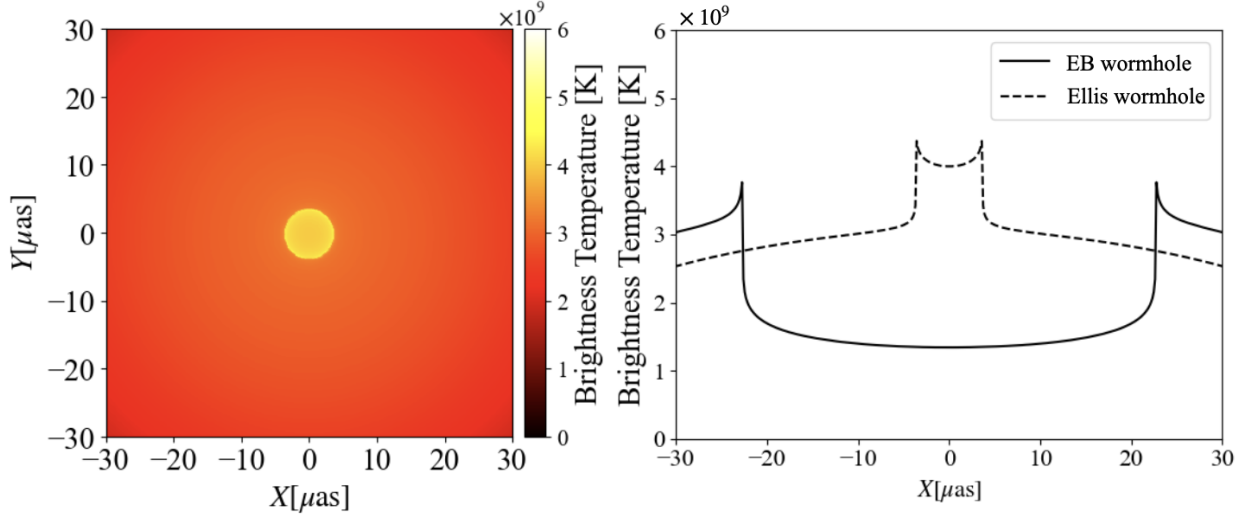


FIG. 7. Simulated image of the Ellis wormhole (left panel) and its intensity profile along the  $Y = 0$  line (right panel). In the right panel, the solid curve is the intensity profile for the EB wormhole, which is the same curve as the solid curve in Fig. 3.

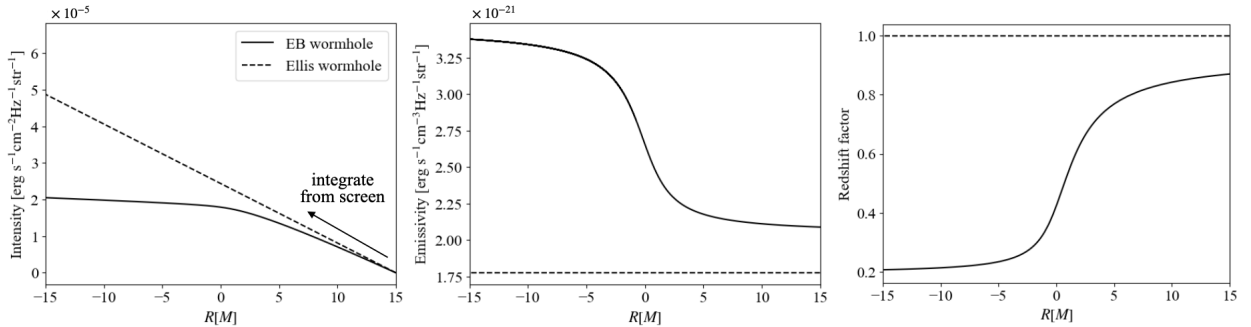


FIG. 8. The observed intensity (left), the emissivity in the fluid rest frame (center), and the redshift factor (right) along the geodesic of a photon that reaches the center of the screen. The solid and dashed curves denote the case of the EB wormhole and the Ellis wormhole, respectively.

if  $u_\infty \neq 0$ , the number density becomes  $n \propto (R^2 + \ell^2)^{-1}$ . On the other hand, we consider the polytropic fluid with  $\Gamma = 4/3$ , where  $\Gamma$  is the adiabatic index. Figure 6 shows the distributions of the electron number density, the electron temperature, the magnetic field strength, and the Lorentz factor for both the Ellis wormhole and the EB wormhole. As seen from the bottom right panel of Fig. 6, in our case, the Lorentz factor of the fluid is not constant for the Ellis wormhole.

Figure 7 shows the simulated image of the Ellis wormhole (left panel) and the intensity profile along the  $Y = 0$  (right panel). We set  $\ell = 1$  in this simulation. For the Ellis wormhole, the region inside the photon ring is brighter than the region outside the photon

ring. This is because the redshift factor for the photons reaching the region inside the photon ring is close to unity in the Ellis wormhole spacetime (see the dashed curve of the right panel in Fig. 8). In the Ellis wormhole, since the lapse function is unity, the redshift factor is primarily determined by the motion of the accreting matter. As seen from the bottom right panel of Fig. 6, the Lorentz factor remains small throughout the spacetime in the Ellis wormhole case, and its variation is small, so that the redshift factor is nearly constant. Furthermore, the emissivity in the fluid rest frame in the Ellis wormhole case is approximately constant with respect to  $R$  (the center panel in Fig. 8). When both the redshift factor and the emissivity are constant, the observed intensity is proportional to the path length of the photon. Therefore, the intensity for the photon reaching the center of the screen increases monotonically in the Ellis wormhole (the left panel in Fig. 8). As a result, the region inside the photon ring is brighter than the region outside the photon ring in the Ellis wormhole.

- 
- [1] Event Horizon Telescope Collaboration, *First M87 Event Horizon Telescope Results. I. The Shadow of the Supermassive Black Hole*, *ApJ* **875** (2019) L1.
  - [2] Event Horizon Telescope Collaboration, *First Sagittarius A\* Event Horizon Telescope Results. I. The Shadow of the Supermassive Black Hole in the Center of the Milky Way*, *ApJL* **930** (2022) L12.
  - [3] Event Horizon Telescope Collaboration, *First Sagittarius A\* Event Horizon Telescope Results. VI. Testing the Black Hole Metric*, *ApJL* **930** (2022) L17.
  - [4] Y. Mizuno, Z. Younsi, C. M. Fromm, O. Porth, M. De Laurentis, H. Olivares, H. Falcke, M. Kramer, and L. Rezzolla, *The current ability to test theories of gravity with black hole shadows*, *Nature Astronomy* **2** (2018) 585 [1804.05812].
  - [5] J. Röder, A. Cruz-Ororio, C. M. Fromm, Y. Mizuno, Z. Younsi, and L. Rezzolla, *Probing the spacetime and accretion model for the Galactic Center: Comparison of Kerr and dilaton black hole shadows*, *A&A* **671** (2023) A143 [2301.09549].
  - [6] K. Moriyama, A. Cruz-Ororio, Y. Mizuno, I. K. Dihingia, and A. Uniyal, *Black hole accretion and radiation variability in general relativistic magnetohydrodynamic simulations with Rezzolla–Zhidenko spacetime*, *A&A* **694** (2025) A135 [2501.08720].

- [7] H. Suzuki, Y. Mizuno, A. Uniyal, I. Kalpa Dihingia, T. Nguyen, and C.-k. Chan, *High-Order Photon Rings around Kerr Naked Singularities*, *arXiv e-prints* (2025) arXiv:2511.20756 [2511.20756].
- [8] M. S. Morris and K. S. Thorne, *Wormholes in space-time and their use for interstellar travel: A tool for teaching general relativity*, *Am. J. Phys.* **56** (1988) 395.
- [9] M. S. Morris, K. S. Thorne, and U. Yurtsever, *Wormholes, Time Machines, and the Weak Energy Condition*, *Phys. Rev. Lett.* **61** (1988) 1446.
- [10] H. G. Ellis, *Ether flow through a drainhole: A particle model in general relativity*, *Journal of Mathematical Physics* **14** (1973) 104.
- [11] K. A. Bronnikov, *Scalar-tensor theory and scalar charge*, *Acta Phys. Polon. B* **4** (1973) 251.
- [12] H.-a. Shinkai and S. A. Hayward, *Fate of the first traversible wormhole: Black hole collapse or inflationary expansion*, *Phys. Rev. D* **66** (2002) 044005 [gr-qc/0205041].
- [13] J. A. Gonzalez, F. S. Guzman, and O. Sarbach, *Instability of wormholes supported by a ghost scalar field. I. Linear stability analysis*, *Class. Quant. Grav.* **26** (2009) 015010 [0806.0608].
- [14] J. A. Gonzalez, F. S. Guzman, and O. Sarbach, *Instability of wormholes supported by a ghost scalar field. II. Nonlinear evolution*, *Class. Quant. Grav.* **26** (2009) 015011 [0806.1370].
- [15] K. A. Bronnikov, J. C. Fabris, and A. Zhidenko, *On the stability of scalar-vacuum space-times*, *Eur. Phys. J. C* **71** (2011) 1791 [1109.6576].
- [16] K. A. Bronnikov, R. A. Konoplya, and A. Zhidenko, *Instabilities of wormholes and regular black holes supported by a phantom scalar field*, *Phys. Rev. D* **86** (2012) 024028 [1205.2224].
- [17] A. Das and S. Kar, *The Ellis wormhole with ‘tachyon matter’*, *Class. Quant. Grav.* **22** (2005) 3045 [gr-qc/0505124].
- [18] A. Shatskiy, I. D. Novikov, and N. S. Kardashev, *New analytic models of ‘traversable’ wormholes*, *Phys. Usp.* **51** (2008) 457 [0810.0468].
- [19] K. A. Bronnikov, L. N. Lipatova, I. D. Novikov, and A. A. Shatskiy, *Example of a stable wormhole in general relativity*, *Grav. Cosmol.* **19** (2013) 269 [1312.6929].
- [20] P. Kanti, B. Kleihaus, and J. Kunz, *Wormholes in Dilatonic Einstein-Gauss-Bonnet Theory*, *Phys. Rev. Lett.* **107** (2011) 271101 [1108.3003].
- [21] P. Kanti, B. Kleihaus, and J. Kunz, *Stable Lorentzian Wormholes in Dilatonic Einstein-Gauss-Bonnet Theory*, *Phys. Rev. D* **85** (2012) 044007 [1111.4049].
- [22] L. Chetouani and G. Clément, *Geometrical optics in the Ellis geometry*, *Gen. Rel. Grav.* **16**

- (1984) 111.
- [23] J. G. Cramer, R. L. Forward, M. S. Morris, M. Visser, G. Benford, and G. A. Landis, *Natural wormholes as gravitational lenses*, *Phys. Rev. D* **51** (1995) 3117 [[astro-ph/9409051](#)].
- [24] D. F. Torres, G. E. Romero, and L. A. Anchordoqui, *Might some gamma-ray bursts be an observable signature of natural wormholes?*, *Phys. Rev. D* **58** (1998) 123001 [[astro-ph/9802106](#)].
- [25] M. Safonova, D. F. Torres, and G. E. Romero, *Microlensing by natural wormholes: Theory and simulations*, *Phys. Rev. D* **65** (2002) 023001 [[gr-qc/0105070](#)].
- [26] M. B. Bogdanov and A. M. Cherepashchuk, *Search for exotic matter from gravitational microlensing observations of stars*, *Astrophys. Space Sci.* **317** (2008) 181 [[0807.2774](#)].
- [27] F. Abe, *Gravitational Microlensing by the Ellis Wormhole*, *Astrophys. J.* **725** (2010) 787 [[1009.6084](#)].
- [28] Y. Toki, T. Kitamura, H. Asada, and F. Abe, *Astrometric Image Centroid Displacements due to Gravitational Microlensing by the Ellis Wormhole*, *Astrophys. J.* **740** (2011) 121 [[1107.5374](#)].
- [29] T. Kitamura, K. Nakajima, and H. Asada, *Demagnifying gravitational lenses toward hunting a clue of exotic matter and energy*, *Phys. Rev. D* **87** (2013) 027501 [[1211.0379](#)].
- [30] N. Tsukamoto and T. Harada, *Light curves of light rays passing through a wormhole*, *Phys. Rev. D* **95** (2017) 024030 [[1607.01120](#)].
- [31] N. Tsukamoto, T. Harada, and K. Yajima, *Can we distinguish between black holes and wormholes by their Einstein ring systems?*, *Phys. Rev. D* **86** (2012) 104062 [[1207.0047](#)].
- [32] G. Clement, *Scattering of Klein-Gordon and Maxwell Waves by an Ellis Geometry*, *Int. J. Theor. Phys.* **23** (1984) 335.
- [33] K. K. Nandi, Y.-Z. Zhang, and A. V. Zakharov, *Gravitational lensing by wormholes*, *Phys. Rev. D* **74** (2006) 024020 [[gr-qc/0602062](#)].
- [34] T. K. Dey and S. Sen, *Gravitational lensing by wormholes*, *Mod. Phys. Lett. A* **23** (2008) 953 [[0806.4059](#)].
- [35] T. Muller, *Exact geometric optics in a Morris-Thorne wormhole spacetime*, *Phys. Rev. D* **77** (2008) 044043.
- [36] A. Bhattacharya and A. A. Potapov, *Bending of light in Ellis wormhole geometry*, *Mod. Phys. Lett. A* **25** (2010) 2399.

- [37] G. W. Gibbons and M. Vyska, *The Application of Weierstrass elliptic functions to Schwarzschild Null Geodesics*, *Class. Quant. Grav.* **29** (2012) 065016 [[1110.6508](#)].
- [38] K. Nakajima and H. Asada, *Deflection angle of light in an Ellis wormhole geometry*, *Phys. Rev. D* **85** (2012) 107501 [[1204.3710](#)].
- [39] N. Tsukamoto and T. Harada, *There are no rotating stars of a perfect fluid in Hořava-Lifshitz gravity*, *Galaxies* **1** (2013) 261 [[1201.1738](#)].
- [40] N. Tsukamoto, *Strong deflection limit analysis and gravitational lensing of an Ellis wormhole*, *Phys. Rev. D* **94** (2016) 124001 [[1607.07022](#)].
- [41] N. Tsukamoto, *Deflection angle in the strong deflection limit in a general asymptotically flat, static, spherically symmetric spacetime*, *Phys. Rev. D* **95** (2017) 064035 [[1612.08251](#)].
- [42] N. Tsukamoto, *Retrolensing by a wormhole at deflection angles  $\pi$  and  $3\pi$* , *Phys. Rev. D* **95** (2017) 084021 [[1701.09169](#)].
- [43] K. Jusufi, *Deflection angle of light by wormholes using the Gauss–Bonnet theorem*, *Int. J. Geom. Meth. Mod. Phys.* **14** (2017) 1750179 [[1706.01244](#)].
- [44] T. Cai, H. Huang, Z. Wang, and M. Zhu, *Higher-order correction to weak-field lensing of an Ellis-Bronnikov wormhole*, *Phys. Rev. D* **108** (2023) 023004 [[2302.13704](#)].
- [45] C. Bambi, *Can the supermassive objects at the centers of galaxies be traversable wormholes? The first test of strong gravity for mm/sub-mm very long baseline interferometry facilities*, *Phys. Rev. D* **87** (2013) 107501 [[1304.5691](#)].
- [46] P. G. Nedkova, V. K. Tinchev, and S. S. Yazadjiev, *Shadow of a rotating traversable wormhole*, *Phys. Rev. D* **88** (2013) 124019 [[1307.7647](#)].
- [47] T. Ohgami and N. Sakai, *Wormhole shadows*, *Phys. Rev. D* **91** (2015) 124020 [[1704.07065](#)].
- [48] T. Ohgami and N. Sakai, *Wormhole shadows in rotating dust*, *Phys. Rev. D* **94** (2016) 064071 [[1704.07093](#)].
- [49] N. Tsukamoto and Y. Gong, *Extended source effect on microlensing light curves by an Ellis wormhole*, *Phys. Rev. D* **97** (2018) 084051 [[1711.04560](#)].
- [50] R. Shaikh, *Shadows of rotating wormholes*, *Phys. Rev. D* **98** (2018) 024044 [[1803.11422](#)].
- [51] S. Paul, R. Shaikh, P. Banerjee, and T. Sarkar, *Observational signatures of wormholes with thin accretion disks*, *JCAP* **03** (2020) 055 [[1911.05525](#)].
- [52] M. A. Bugaev, I. D. Novikov, S. V. Repin, and A. A. Shelkovernikova, *Gravitational Lensing and Wormhole Shadows*, *Astron. Rep.* **65** (2021) 1185 [[2106.03256](#)].

- [53] V. A. Ishkaeva and S. V. Sushkov, *Image of an accreting general Ellis-Bronnikov wormhole*, *Phys. Rev. D* **108** (2023) 084054 [[2308.02268](#)].
- [54] H. Huang, J. Kunz, J. Yang, and C. Zhang, *Light ring behind wormhole throat: Geodesics, images, and shadows*, *Phys. Rev. D* **107** (2023) 104060 [[2303.11885](#)].
- [55] M. Alloqulov, F. Atamurotov, A. Abdujabbarov, B. Ahmedov, and V. Khamidov, *Shadow and weak gravitational lensing for Ellis-Bronnikov wormhole*, *Chin. Phys. C* **48** (2024) [025104](#).
- [56] I. D. Novikov, S. V. Repin, and D. A. Paksivatova, *Observing an accretion disk inside a wormhole shadow*, [2508.02752](#).
- [57] J. ze Xia, H. xuan Jiang, C. Liu, and Y. Mizuno, *Dynamics and radiative signatures of accretion flows onto a kerr-like wormhole*, [2605.04631](#).
- [58] V. A. Ishkaeva and S. V. Sushkov, *Image of a wormhole with an arbitrary throat profile*, [2605.16413](#).
- [59] R. Takahashi and M. Umemura, *General relativistic radiative transfer code in rotating black hole space – time : ARTIST*, *MNRAS* **4585** (2017) 4567.
- [60] M. M. Takahashi, K. Ohsuga, R. Takahashi, T. Ogawa, M. Umemura, and Y. Asahina, *3D photon conserving code for time-dependent general relativistic radiative transfer: CARTOON*, *MNRAS* **517** (2022) 3711 [[2210.00686](#)].
- [61] R. Mahadevan, R. Narayan, and I. Yi, *Harmony in Electrons: Cyclotron and Synchrotron Emission by Thermal Electrons in a Magnetic Field*, *ApJ* **465** (1996) 327 [[astro-ph/9601073](#)].
- [62] H.-Y. Pu, K. Yun, Z. Younsi, and S.-J. Yoon, *Odyssey: A Public GPU-based Code for General Relativistic Radiative Transfer in Kerr Spacetime*, *ApJ* **820** (2016) 105 [[1601.02063](#)].
- [63] A. Pandya, Z. Zhang, M. Chandra, and C. F. Gammie, *Polarized Synchrotron Emissivities and Absorptivities for Relativistic Thermal, Power-law, and Kappa Distribution Functions*, *ApJ* **822** (2016) 34 [[1602.08749](#)].
- [64] J. Dexter, *A public code for general relativistic, polarised radiative transfer around spinning black holes*, *MNRAS* **462** (2016) 115.
- [65] EVENT HORIZON TELESCOPE) collaboration, *Verification of Radiative Transfer Schemes for the EHT*, *Astrophys. J.* **897** (2020) 148.

- [66] T. Kawashima, K. Ohsuga, and H. R. Takahashi, *RAIKOU: A General Relativistic, Multiwavelength Radiative Transfer Code*, *ApJ* **949** (2023) 101 [2108.05131].
- [67] M. M. Takahashi, T. Kawashima, and K. Ohsuga, *Black hole spin estimation with time-variable image of M 87 during the flaring state*, *PASJ* **78** (2026) 298 [2511.18410].
- [68] K. Gebhardt and J. Thomas, *The Black Hole Mass, Stellar Mass-to-Light Ratio, and Dark Halo in M87*, *Astrophys. J.* **700** (2009) 1690 [0906.1492].
- [69] S. Bird, W. E. Harris, J. P. Blakeslee, and C. Flynn, *The inner halo of M 87: a first direct view of the red-giant population*, *A&A* **524** (2010) A71 [1009.3202].
- [70] K. Gebhardt, J. Adams, D. Richstone, T. R. Lauer, S. M. Faber, K. Gültekin, J. Murphy, and S. Tremaine, *The Black Hole Mass in M87 from Gemini/NIFS Adaptive Optics Observations*, *ApJ* **729** (2011) 119 [1101.1954].
- [71] Event Horizon Telescope Collaboration, *First M87 Event Horizon Telescope Results. VII. Polarization of the Ring*, *ApJL* **910** (2021) L12.
- [72] Event Horizon Telescope Collaboration, *First M87 Event Horizon Telescope Results. VIII. Magnetic Field Structure near The Event Horizon*, *ApJL* **910** (2021) L13.
- [73] M. D. Johnson *et al.*, *The Black Hole Explorer: motivation and vision*, *Proc. SPIE Int. Soc. Opt. Eng.* **13092** (2024) 130922D [2406.12917].
- [74] K. Akiyama *et al.*, *The Japanese vision for the Black Hole Explorer mission*, *Proc. SPIE Int. Soc. Opt. Eng.* **13092** (2024) 130922E [2406.09516].
- [75] T. Kawashima, Y. Tsunetoe, K. Ohsuga, M. Kino, Y. Mizuno, K. Moriyama, H. Saida, K. Akiyama, K. Hada, and K. Niinuma, *Black hole spacetime and properties of accretion flows and jets probed by Black Hole Explorer: science cases proposed by BHEX Japan team*, *Proc. SPIE Int. Soc. Opt. Eng.* **13092** (2024) 130926X [2406.09995].